nanomaterials

MDPI

Article

Gold Nanorod-Decorated Metallic MoS_2 Nanosheets for Synergistic Photothermal and Photodynamic Antibacterial Therapy

Sibidou Yougbaré [1,2,†], Chinmaya Mutalik [1,†], Pei-Feng Chung [3], Dyah Ika Krisnawati [4], Fajar Rinawati [4], Hengky Irawan [4], Heny Kristanto [4] and Tsung-Rong Kuo [1,5,*]

1 International Ph.D. Program in Biomedical Engineering, College of Biomedical Engineering, Taipei Medical University, Taipei 11031, Taiwan; d845107003@tmu.edu.tw (S.Y.); d845108002@tmu.edu.tw (C.M.)
2 Institut de Recherche en Sciences de la Santé (IRSS-DRCO)/Nanoro, 03 B.P 7192, Ouagadougou 03, Burkina Faso
3 School of Biomedical Engineering, College of Biomedical Engineering, Taipei Medical University, Taipei 11031, Taiwan; b812107004@tmu.edu.tw
4 Dharma Husada Nursing Academy, Kediri 64114, Indonesia; dyah_ika_k@adhkediri.ac.id (D.I.K.); fajar_rinawati@adhkediri.ac.id (F.R.); hengky_irawan@adhkediri.ac.id (H.I.); heny_kristanto@adhkediri.ac.id (H.K.)
5 Graduate Institute of Nanomedicine and Medical Engineering, College of Biomedical Engineering, Taipei Medical University, Taipei 11031, Taiwan
* Correspondence: trkuo@tmu.edu.tw
† These authors contributed equally to this work.

Abstract: Light-responsive nanocomposites have become increasingly attractive in the biomedical field for antibacterial applications. Visible-light-activated metallic molybdenum disulfide nanosheets (1T-MoS_2 NSs) and plasmonic gold nanorods (AuNRs) with absorption at a wavelength of 808 nm were synthesized. AuNR nanocomposites decorated onto 1T-MoS_2 NSs (MoS_2@AuNRs) were successfully prepared by electrostatic adsorption for phototherapy applications. Based on the photothermal effect, the solution temperature of the MoS_2@AuNR nanocomposites increased from 25 to 66.7 °C after 808 nm near-infrared (NIR) laser irradiation for 10 min. For the photodynamic effect, the MoS_2@AuNR nanocomposites generated reactive oxygen species (ROS) under visible light irradiation. Photothermal therapy and photodynamic therapy of MoS_2@AuNRs were confirmed against *E. coli* by agar plate counts. Most importantly, the combination of photothermal therapy and photodynamic therapy from the MoS_2@AuNR nanocomposites revealed higher antibacterial activity than photothermal or photodynamic therapy alone. The light-activated MoS_2@AuNR nanocomposites exhibited a remarkable synergistic effect of photothermal therapy and photodynamic therapy, which provides an alternative approach to fight bacterial infections.

Keywords: antimicrobial activity; gold nanorods; metallic molybdenum disulfide; phototherapy; photothermal therapy; photodynamic therapy; synergistic effect

Citation: Yougbaré, S.; Mutalik, C.; Chung, P.-F.; Krisnawati, D.I.; Rinawati, F.; Irawan, H.; Kristanto, H.; Kuo, T.-R. Gold Nanorod-Decorated Metallic MoS_2 Nanosheets for Synergistic Photothermal and Photodynamic Antibacterial Therapy. *Nanomaterials* **2021**, *11*, 3064. https://doi.org/10.3390/nano11113064

Academic Editor: Krasimir Vasilev

Received: 21 October 2021
Accepted: 12 November 2021
Published: 14 November 2021

1. Introduction

Photoresponsive nanomaterials have been extensively applied for energy conversion, electronic devices, and medical therapies [1–8]. Recently, the use of light-activated nanomaterials has been focused on phototherapy [9–16]. Phototherapy is defined as the use of photoresponsive nanomaterials to generate heat or noxious components to kill microorganisms or cells [17–19]. For phototherapy, there are two main approaches: photothermal therapy and photodynamic therapy [20–22]. Photothermal therapy is a treatment that utilizes photothermal agents activated by light irradiation. The absorbed light energy is transformed into heat by photothermal agents for therapeutic purposes [23–25]. Photothermal therapy was reported to induce no bacterial resistance, and therefore, it is effective

against superbugs [26]. With photodynamic therapy, light-activated nanomaterials absorb light to facilitate the generation of reactive oxygen species (ROS) [27–30]. Light-induced ROS production by nanomaterials can destroy bacteria via two main mechanisms. First, ROS can bind to bacterial membranes, inducing destruction of bacterial cell walls. Second, ROS can penetrate bacterial cells to bind to and damage lipids and proteins and thus disrupt cell physiological activities, leading to bacterial death [31]. Although light-activated nanomaterials have been demonstrated for both photothermal therapy and photodynamic therapy, designing nanomaterials to provide a synergistic effect of photothermal therapy and photodynamic therapy is still an emerging task in medical therapeutics.

Different photothermal agents such as metals, metal oxides, and carbon nanomaterials have been investigated for photothermal therapy [32–34]. For instance, gold nanorods (AuNRs) and gold nanobipyramids were verified to be photothermal agents with highly efficient antibacterial activities [35]. A nanocomposite composed by polyurethane, polyethylene glycol, and AuNRs was prepared as a near-infrared (NIR)-responsive organic/inorganic hybrid to fight multidrug-resistant (MDR) bacteria [36]. Polypyrrole coated with Fe_3O_4 nanocomposites was demonstrated to increase the temperature of tumors from 32.8 to 48.8 °C within 5 min under 808 nm NIR laser irradiation [37]. Polypyrrole-based photothermal nanoantibiotics with robust photothermal effects in the NIR-II region (~1064 nm) were designed for valid treatment of MDR bacterial infections [38]. Among these photothermal agents, plasmonic metal nanomaterials have been intensively investigated because of their superior photothermal effects. More interestingly, photothermal therapy has been combined with other therapies such as photodynamic therapy, chemotherapy, radiotherapy, and so on for better therapeutic outcomes.

Various light-activated nanomaterials are popularly applied as antibacterial agents based on photodynamic therapy [39–45]. For example, metallic molybdenum disulfide (1T-MoS_2) and semiconducting molybdenum disulfide (2H-MoS_2) nanoflowers were validated to have bactericidal effects due to their light-driven ROS production [46]. A nanocomposite of iron disulfide nanoparticles (NPs) conjugated with titanium dioxide NPs was designed as a photodynamic antibacterial agent with broad absorption from the visible (Vis) to NIR region [47]. A nanocomposite of zinc oxide NPs doped with selenium was fabricated as an antibacterial nanomedicine to provide ROS to inhibit the growth of *S. aureus* under visible light illumination [48]. Graphene oxide–cuprous oxide heterostructured nanocomposites were synthesized with long-term antibacterial activity against *E. coli* and *S. aureus*; they utilized the synergistic effect of light-induced ROS production and the sustained release of copper ions [49]. Currently, great achievements have been made in applications of light-activated nanomaterials for photodynamic therapy. However, to enhance therapeutic efficiencies, nanocomposites with a synergistic effect of photothermal therapy and photodynamic therapy are still being developed.

In this work, a seed mediation approach was applied to prepare plasmonic AuNRs. Nanosheets (NSs) of 1T-MoS_2 were prepared via a facile solvothermal method. Afterward, AuNRs were decorated onto the 1T-MoS_2 NSs (MoS_2@AuNRs) by electrostatic adsorption for use as an antibacterial agent in a phototherapy application. AuNRs, 1T-MoS_2 NSs, and MoS_2@AuNRs were characterized by ultraviolet (UV)–Vis spectroscopy, transmission electron microscopy (TEM), zeta potential, Fourier transform infrared (FTIR) spectroscopy, and powder X-ray diffraction (XRD) to confirm their optical and structural properties. The photothermal effect and photodynamic effect of MoS_2@AuNRs were respectively investigated using an NIR laser and visible light irradiation. The photothermal therapy and photodynamic therapy of MoS_2@AuNRs were separately examined against *E. coli* by agar plate counts. The synergistic effect of photothermal therapy and photodynamic therapy from MoS_2@AuNRs was also evaluated as an antibacterial application.

2. Methods

2.1. Chemicals

Hexadecyltrimethylammonium bromide (CTAB, ≥98.0%), hydrogen tetrachloroaurate(III) ($HAuCl_4 \cdot 3H_2O$), sodium borohydride ($NaBH_4$), oleic acid (≥99%), silver nitrate ($AgNO_3$), L-ascorbic acid (99%), a hydrochloric acid solution (HCl, 12 M), thiourea (>99%), molybdic acid (≥85.0% MoO_3 basis), 2′,7′-dichlorofluorescein diacetate (H2DCFDA), and ethanol were purchased from Sigma-Aldrich (St. Louis, MO, USA). Phosphate-buffered saline (PBS; 1×, pH 7.4) was purchased from Bioshop (Burlington, ON, Canada). All chemicals were purchased and used without further purification.

2.2. Synthesis of AuNRs via a Seed-Mediation Method

AuNRs were prepared according to a seed-mediation method used in our previous work [35]. For the seed-mediation method, a seed solution and growth solution were first prepared. The seed solution was prepared by adding 100 µL of a $HAuCl_4$ (25 mM) aqueous solution to 10 mL of a CTAB aqueous solution (0.1 M) with stirring at 30 °C. Afterward, 2 mL of a fresh, ice-cold $NaBH_4$ (6 mM) aqueous solution was added to the seed solution, and then the seed solution was further stirred for 2 min. Before being added to the growth solution, the seed solution was stored for 2 h at room temperature in the dark. The growth solution (25 mL) was composed by CTAB (0.2 M) and oleic acid (0.035 M). Furthermore, 4.8 mL of an $AgNO_3$ aqueous solution (4 mM) was added to the growth solution with stirring for 15 min, and then a $HAuCl_4$ aqueous solution (50 mL, 1 mM) was also poured into the growth solution with stirring at 30 °C for 90 min. Afterward, the colorless growth solution was added to the HCl solution (190 µL, 12 M) for further reaction for 15 min. Finally, the growth solution was added to an ascorbic acid aqueous solution (310 µL, 0.1 M) with stirring. To synthesize AuNRs, the seed solution (35 µL) was injected into growth solution with stirring. Subsequently, the mixture of seed solution and growth solution was placed for AuNR growth overnight. For purification, the rust-red AuNR solution was centrifuged at 6000 rpm for 10 min. After centrifugation, the supernatant was carefully poured out, and the AuNR precipitate was redispersed in the CTAB solution (2 mM).

2.3. Preparation of 1T-MoS_2 NSs

NSs of 1T-MoS_2 were prepared according to a solvothermal method with some modifications [46]. Typically, a precursor solution (40 mL) containing thiourea (12.5 mM) and molybdic acid (5 mM) was prepared with stirring. After stirring for 30 min, 100 mL of the precursor solution was transferred to a PTFE-lined stainless-steel autoclave. Afterward, the autoclave was sealed and heated to 180 °C in an oven. After reacting for 24 h, the autoclave reactor was cooled to room temperature. Eventually, 1T-MoS_2 NSs were prepared. For further application, 1T-MoS_2 NSs were washed with water and ethanol several times and then dried at 60 °C in an oven overnight to produce black powder.

2.4. Synthesis of AuNR-Decorated 1T-MoS_2 NSs

A 1T-MoS_2 NS aqueous solution at a concentration of 100 µg/mL was prepared. AuNR aqueous solutions of three different concentrations of 100, 50, and 33.3 µg/mL were prepared in CTAB aqueous solutions (125 µM). To prepare AuNR-decorated 1T-MoS_2 NSs, three samples of the 1T-MoS_2 NS solution (500 µL, 100 µg/mL) were introduced into 500 µL of AuNR solutions with various concentrations of 100 µg/mL (MoS_2@AuNRs), 50 µg/mL (MoS_2@1/2AuNRs), and 33.3 µg/mL (MoS_2@1/3AuNRs). The three solutions, one each of MoS_2@AuNRs, MoS_2@1/2AuNRs, and MoS_2@1/3AuNRs, were then mixed at 26 °C with shaking for 3 h. After 3 h, the three solutions were centrifuged at 5000 rpm for 10 min, the supernatants were discarded, and the precipitates were further dissolved in 500 µL of a PBS solution by sonication for 5 min. Samples of MoS_2@AuNR, MoS_2@1/2AuNR, and MoS_2@1/3AuNR solutions were stored at 4 °C until being used in subsequent experiments.

2.5. Photothermal Performance of MoS_2@AuNRs

Photothermal performances were investigated using an 808 nm NIR laser (DPSSL DRIVER II) (ONSET, New Taipei City, Taiwan) with a power intensity of 1 W/cm^2. Three samples, one each of MoS_2@AuNRs, MoS_2@1/2AuNRs, and MoS_2@1/3AuNRs (400 µL), were separately added into microplate wells. Each sample was irradiated for 10 min, and the sample temperature was measured every minute with a thermal imaging camera during 808 nm NIR laser irradiation.

2.6. Evaluation of ROS Generation by MoS_2@AuNRs

ROS generation was evaluated with a dichlorofluorescein assay. In the presence of ROS, 2′,7′-dichlorodihydrofluorescein diacetate (H2DCFDA) was oxidized to form 2′,7′-dichlorofluorescein (DCF). H2DCFDA does not fluoresce, while DCF does. The fluorescence intensity of DCF was quantitatively detected by fluorescence spectroscopy using excitation/emission at 488/525 nm. The fluorescence intensity of DCF was proportional to the concentration of ROS production. The working solution was obtained by means of PBS and two intermediate solutions named solutions I and II. Solution I was prepared by adding 4.87 mg of H2DCFDA to 10 mL of ethanol (99.5%). Sodium hydroxide (0.01 mM) was prepared as solution II. The working solution was a mixture of 10 mL of PBS, 2 mL of solution I, and 2 mL of solution II, and it was incubated for 30 min while being protected from light. After incubation, the solution was ready to use or could be stored at 4 °C. The total ROS generated were evaluated by the fluorescence intensity developed by a mixture of 1 mL of the working solution and 200 µL of the sample.

2.7. Antibacterial Phototherapy of E. coli

The effect of antimicrobial phototherapy of MoS_2@AuNRs on *E. coli* was evaluated using the agar plate counting method. Briefly, three samples, one each of MoS_2@AuNRs, MoS_2@1/2AuNRs, and MoS_2@1/3AuNRs (250 µL), were respectively added to 250 µL of an *E. coli* suspension with an optical density at 600 nm (OD_{600}) of 0.2. These three mixtures separately underwent three types of light exposure, including an 808 nm NIR laser at a power density at 1.0 W/cm^2, visible light, and both. Simulated solar AM1.5 light (xenon lamp, Enlitech LH150) (Enlitech, Kaohsiung City, Taiwan) was applied as the visible light source. After light exposure, these three mixtures were further cultured at 37 °C for 3 h. Afterward, 20 µL of each mixture was cultured on LB agar plates at 37 °C for 18 h.

3. Results and Discussion

3.1. Optical Properties of MoS_2@AuNRs

The optical properties of 1T-MoS_2 NSs, AuNRs, and MoS_2@AuNRs were first characterized by UV–Vis spectroscopy. In the UV–Vis spectrum shown in Figure 1a, 1T-MoS_2 NSs revealed two excitonic absorption bands located at wavelengths of 438 and 588 nm, corresponding to the metallic phase of MoS_2 [50,51]. As shown in Figure 1b, the UV–Vis spectrum of the AuNRs exhibited transverse and longitudinal surface plasmon resonance (SPR) bands with maximal absorptions at ~520 and ~808 nm, respectively. For AuNRs decorated with 1T-MoS_2 NSs, the UV–Vis absorption spectra of the nanocomposites, including MoS_2@1/3AuNRs, MoS_2@1/2AuNRs, and MoS_2@AuNRs, revealed a noticeable red-shift of the longitudinal SPR band compared to that of the AuNRs, as shown in Figure 1c. The redshifts of the longitudinal SPR band for the MoS_2@1/3AuNRs, MoS_2@1/2AuNRs, and MoS_2@AuNRs were 67, 101, and 117 nm, respectively. Furthermore, band broadening of the longitudinal SPR bands of AuNRs was also observed in MoS_2@1/3AuNRs, MoS_2@1/2AuNRs, and MoS_2@AuNRs. The red-shift and broadening of the longitudinal SPR band of AuNRs in MoS_2@1/3AuNRs, MoS_2@1/2AuNRs, and MoS_2@AuNRs could be attributed to changes in the surface refractive index of the AuNRs after decoration with 1T-MoS_2 NSs [52]. Although the red-shift and broadening of the longitudinal SPR band were observed, the MoS_2@1/3AuNR, MoS_2@1/2AuNR, and MoS_2@AuNR nanocomposites still clearly exhibited absorption at 808 nm. The absorption intensities of the MoS_2@1/3AuNRs,

MoS_2@1/2AuNRs, and MoS_2@AuNRs were 0.059, 0.105, and 0.113, respectively, at 808 nm. With absorption at 808 nm, the MoS_2@1/3AuNR, MoS_2@1/2AuNR, and MoS_2@AuNR nanocomposites were further applied as photothermal agents.

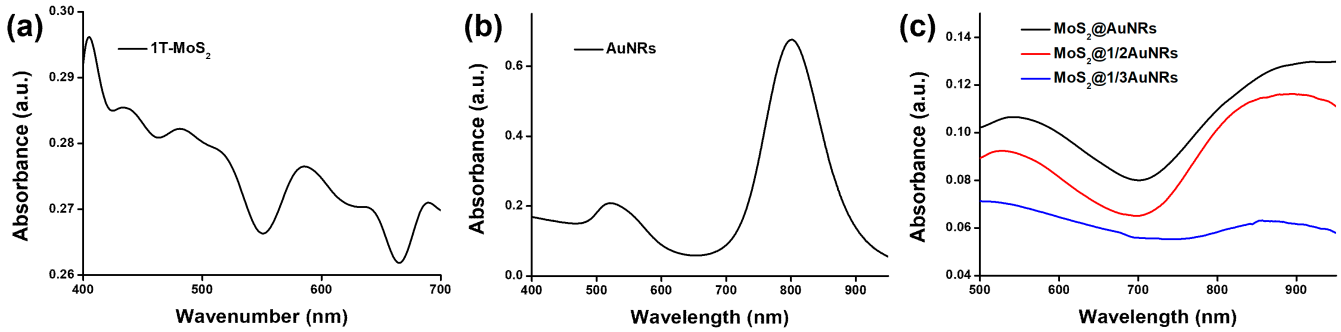

Figure 1. UV–Vis absorption spectra of (**a**) metallic molybdenum disulfide (1T-MoS_2) nanosheets (NSs), (**b**) gold nanorods (AuNRs), (**c**) MoS_2@1/3AuNRs, MoS_2@1/2AuNRs, and MoS_2@AuNRs.

3.2. Structural Characterization of MoS_2@AuNRs

The morphologies of 1T-MoS_2 NSs, AuNRs, and MoS_2@AuNRs were examined on TEM images. In the TEM image shown in Figure 2a, the NS structure of 1T-MoS_2 NSs can be observed. The white arrows indicate different thin layers of the 1T-MoS_2 NSs. As shown in Figure 2b, the aspect ratio (length/diameter) of the AuNRs was calculated to be 4.32, according to the average length (80.7 nm) and diameter (18.7 nm). After calculating based on the AuNRs in the TEM image, the synthetic yield we obtained exceeded 95%. As shown in Figure 2c, AuNRs were randomly decorated on the surface of 1T-MoS_2 NSs. The zeta potentials of 1T-MoS_2 NSs and AuNRs were negative (–32.7 mV) and positive (44.6 mV), respectively. Therefore, for MoS_2@AuNRs, the decoration of AuNRs on 1T-MoS_2 NSs could be attributed to electrostatic adsorption [53,54]. Overall, the results of TEM characterization indicated that MoS_2@AuNRs were successfully prepared by electrostatic adsorption between AuNRs and 1T-MoS_2 NSs.

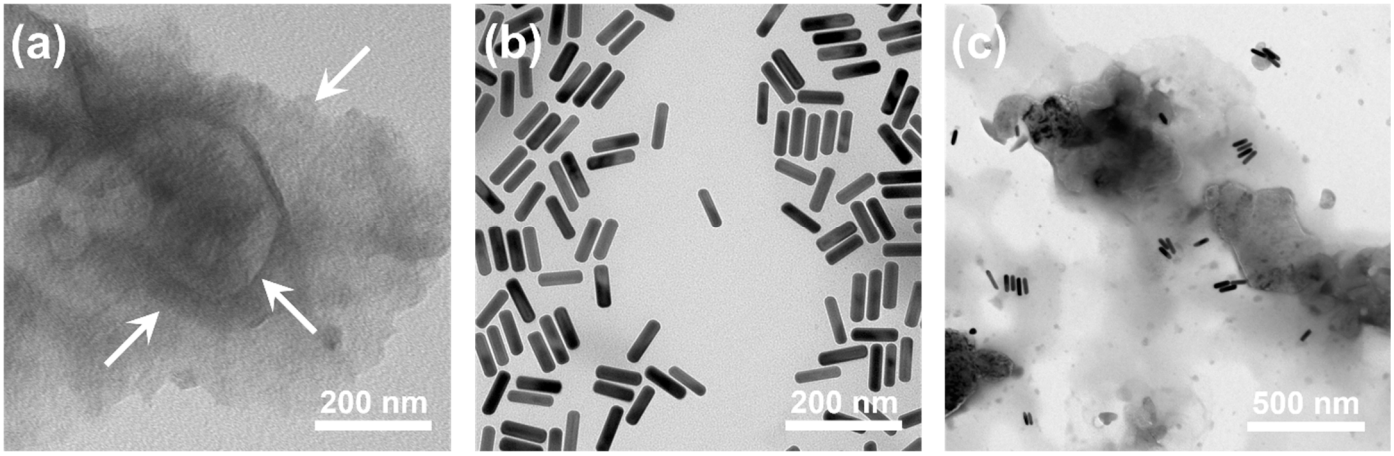

Figure 2. TEM images of (**a**) metallic molybdenum disulfide (1T-MoS_2) nanosheets (NSs), (**b**) gold nanorods (AuNRs), and (**c**) MoS_2@AuNRs.

3.3. FTIR Characterization of MoS_2@AuNRs

The anchoring of AuNRs onto 1T-MoS_2 NSs was also investigated by FTIR from 400 to 4000 cm^{-1}. First, the FTIR spectra of 1T-MoS_2 NSs and AuNRs were examined and compared to that of MoS_2@AuNRs. As shown in Figure 3, the FTIR spectrum of 1T-MoS_2 NSs revealed a broad band at 3200 cm^{-1} because of OH stretching of hydrogen bonds [55].

Characteristic peaks at 1616, 1424, 1106, 880, and 615 cm^{-1} were ascribed to 1T-MoS_2 NSs. For the FTIR spectrum of AuNRs, the strong, broad band at 3400 cm^{-1} was provided by OH stretching of the adsorbed H_2O [56]. A bending band of H_2O was observed at 1640 cm^{-1}. Moreover, the weak band at 1195 cm^{-1} was indexed as CN stretching of CTAB. The FTIR spectrum of AuNRs indicated that the CTAB surfactant was conjugated onto the surface of AuNRs. Most importantly, characteristic FTIR peaks of 1T-MoS_2 NSs and AuNRs were observed in the FTIR spectrum of MoS_2@AuNRs. The FTIR characterization indicated that there were no significant changes in 1T-MoS_2 NSs or AuNRs after their decoration.

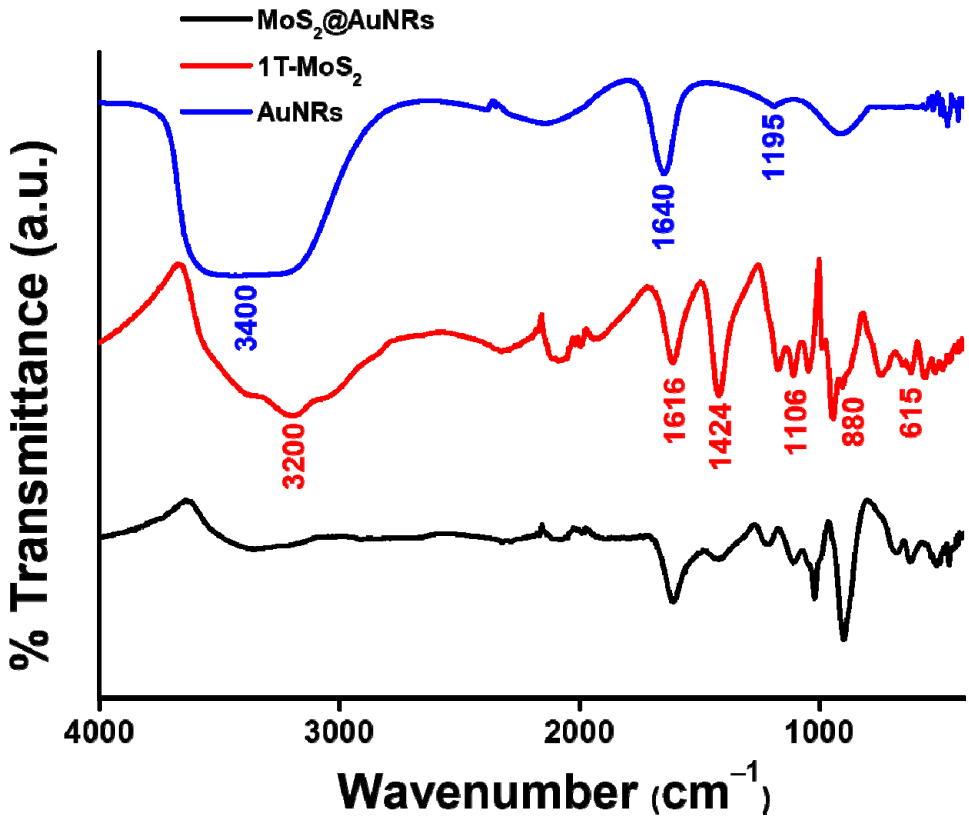

Figure 3. FTIR spectra of gold nanorods (AuNRs), metallic molybdenum disulfide (1T-MoS_2) nanosheets (NSs), and MoS_2@AuNRs.

3.4. XRD Investigation of MoS_2@AuNRs

XRD spectra were measured to identify the crystallinity of the nanocomposites, including AuNRs, 1T-MoS_2 NSs, and MoS_2@AuNRs. As shown in Figure 4, the XRD spectrum of 1T-MoS_2 NSs revealed two critical peaks at 9.6° and 19.1°, corresponding to the crystal planes of (002) and (004) of the 1T-MoS_2 NSs (JCPDS No. 37-1492), respectively [57]. The XRD pattern of AuNRs revealed three main XRD peaks located at 38.2°, 44.4°, and 64.6°, corresponding to the crystal planes of (111), (200), and (220), respectively [58,59]. For MoS_2@AuNRs, characteristic peaks of 1T-MoS_2 NSs and AuNRs were still exhibited after the decoration of AuNRs onto 1T-MoS_2 NSs. Results of the XRD investigation demonstrated that the crystal structures of 1T-MoS_2 NSs and AuNRs were retained in the MoS_2@AuNR nanocomposite.

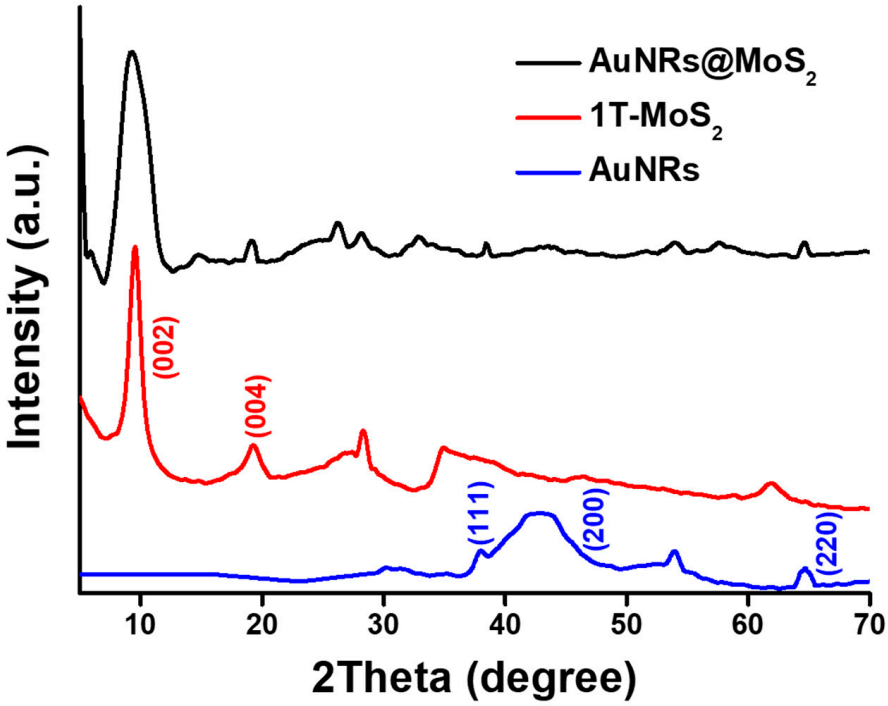

Figure 4. XRD spectra of gold nanorods (AuNRs), metallic molybdenum disulfide (1T-MoS_2) nanosheets (NSs), and MoS_2@AuNRs.

3.5. Photothermal Performance of MoS_2@AuNRs

To compare photothermal performances, 1T-MoS_2 NSs, AuNRs, MoS_2@AuNRs, MoS_2 @1/2AuNRs, and MoS_2@1/3AuNRs were illuminated by an 808 nm NIR laser. For the control experiments, the temperature of sterilized water revealed no significant increase under NIR laser irradiation, as shown in Figure 5a. After NIR laser irradiation for 10 min, the temperature of the 1T-MoS_2 NS solution (100 μg/mL) increased from 25.0 to 54.2 °C. Moreover, as shown in Figure 5b, the temperature of the control (CTAB aqueous solution, 125 μM) showed no obvious increase under NIR laser irradiation. After NIR laser irradiation for 10 min, the temperature of the AuNR solution (100 μg/mL) increased from 25.0 to 57.6 °C. As shown in Figure 5c, the temperature of the control (PBS solution) indicated no significant increase under NIR laser irradiation. Furthermore, the final temperatures of the MoS_2@AuNRs, MoS_2@1/2AuNRs, and MoS_2@1/3AuNRs were 66.7, 62.9, and 59.5 °C, respectively, after NIR laser illumination for 10 min. The results of the photothermal assays demonstrated that the photothermal performance of MoS_2@AuNR nanocomposites increased with the concentration of AuNRs. Most importantly, with the decoration of AuNRs onto 1T-MoS_2 NSs, MoS_2@AuNR nanocomposites exhibited higher photothermal performance that that of 1T-MoS_2 NSs or AuNRs. The reason could be attributed to the synergistic photothermal effect between the 1T-MoS_2 NS and AuNRs in MoS_2@AuNR nanocomposites. For photothermal therapy, a minimum temperature of 50 °C was able to destroy *E. coli* [35]. The temperature of the MoS_2@AuNR solution reached 50 °C with NIR laser illumination for 2 min. Therefore, an irradiation time of 2 min was set for MoS_2@AuNRs in the following application of photothermal therapy.

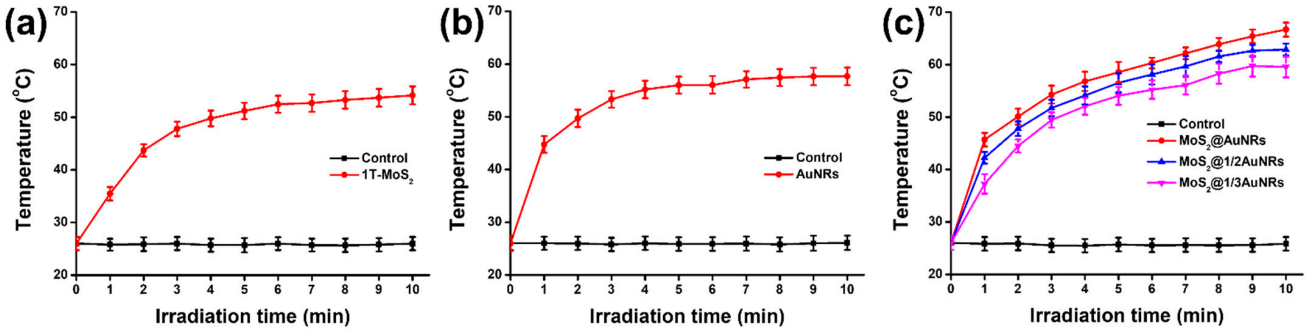

Figure 5. Photothermal performances of (**a**) metallic molybdenum disulfide (1T-MoS_2) nanosheets (NSs), (**b**) gold nanorods (AuNRs), and (**c**) MoS_2@AuNRs, MoS_2@1/2AuNRs, and MoS_2@1/3AuNRs. Sterilized water, CTAB aqueous solution (125 μM), and PBS solution were applied as the controls in (**a**), (**b**), and (**c**), respectively. All data are presented as the mean ± SD, $n = 3$ per group.

3.6. ROS Generation by MoS_2@AuNRs

To examine photodynamic performance, the ROS generated by 1T-MoS_2 NSs, AuNRs, and MoS_2@AuNRs were investigated under NIR laser and visible light irradiation based on the H2DCFDA assay. As shown in Figure 6, the ROS levels of 1T-MoS_2 NSs, AuNRs, and MoS_2@AuNRs without irradiation were set to 1.0. As shown in Figure 6a, the relative ROS levels of 1T-MoS_2 NSs with NIR laser (2 min), visible light (1 min), and both NIR laser (2 min) and visible light (1 min) irradiation were respectively 1.23-, 4.25-, and 5.43-fold higher compared to that of no irradiation. The results could be because metallic 1T-MoS_2 NSs with photocatalytic activity induced the ROS generation under visible light [46]. However, for the AuNRs, with NIR laser, visible light, and both NIR laser and visible light irradiation, there were no significant increases in ROS production, as shown in Figure 6b. Most importantly, the relative ROS levels of MoS_2@AuNRs with NIR laser, visible light, and both NIR laser and visible light irradiation were 1.53-, 5.06-, and 5.81-fold higher, respectively, compared to that of no irradiation as shown in Figure 6c. With NIR laser irradiation, there was no significant production of ROS from MoS_2@AuNRs because very few light-induced ROS were generated by the 1T-MoS_2 NSs and AuNRs. However, with visible light irradiation, remarkable light-induced ROS production from MoS_2@AuNRs was measured due to the visible-light activity of the 1T-MoS_2 NSs. Furthermore, with both NIR laser and visible light irradiation, the light-induced ROS production from the MoS_2@AuNRs did not noticeably increase compared to that of MoS_2@AuNRs with only visible light irradiation. The reason could be the light-induced ROS production from MoS_2@AuNRs mainly being contributed by the visible-light activity of the 1T-MoS_2 NSs in the MoS_2@AuNRs.

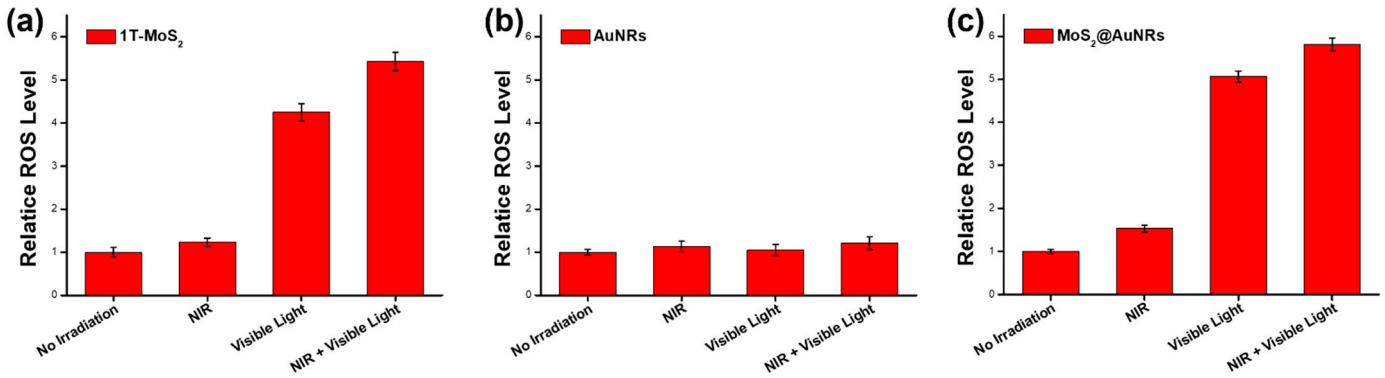

Figure 6. Relative reactive oxygen species (ROS) levels of (**a**) metallic molybdenum disulfide (1T-MoS_2) nanosheets (NSs), (**b**) gold nanorods (AuNRs), and (**c**) MoS_2@AuNRs with no light irradiation and with near infrared (NIR) laser, visible light, and both NIR laser and visible light irradiation. All data are presented as the mean ± SD, $n = 3$ per group.

3.7. Evaluation of Photothermal Therapy and Photodynamic Therapy of MoS_2@AuNRs

To evaluate the performance of photothermal therapy and photodynamic therapy, the light-induced bactericidal activities of MoS_2@1/3AuNRs, MoS_2@1/2AuNRs, and MoS_2@AuNRs were investigated by agar plate counts. As shown in Figure 7, with NIR laser irradiation for 2 min, bacterial reductions by MoS_2@1/3AuNRs, MoS_2@1/2AuNRs, and MoS_2@AuNRs were 84.4%, 97.5%, and 99.0%, respectively. The results indicated that an increase in AuNRs decorating 1T-MoS_2 NSs improved the photothermal effect of the MoS_2@1/3AuNR, MoS_2@1/2AuNR, and MoS_2@AuNR nanocomposites. Therefore, with the highest concentration of AuNRs, MoS_2@AuNRs exhibited the best photothermal therapy compared to MoS_2@1/3AuNRs and MoS_2@1/2AuNRs. With visible light irradiation (1 min), the antibacterial rates of MoS_2@1/3AuNRs, MoS_2@1/2AuNRs, and MoS_2@AuNRs were 83.8%, 93.3%, and 98.5%, respectively. Under visible light irradiation, the antibacterial activities of MoS_2@1/3AuNRs, MoS_2@1/2AuNRs, and MoS_2@AuNRs were attributed to their light-induced ROS generation. Most importantly, to investigate the synergistic effect of photothermal therapy and photodynamic therapy, MoS_2@1/3AuNRs, MoS_2@1/2AuNRs, and MoS_2@AuNRs were sequentially irradiated with NIR laser and visible light. After irradiation with NIR laser and visible light, the bactericidal efficiencies of MoS_2@1/3AuNRs, MoS_2@1/2AuNRs, and MoS_2@AuNRs were 94.5%, 100%, and 100%, respectively. With the combination of NIR laser and visible light irradiation, significant increases in bactericidal efficiencies were demonstrated compared to irradiation by only the NIR laser or visible light. Overall, with the decoration of the photothermal agent of AuNRs onto the photodynamic agent of 1T-MoS_2 NSs, the synergistic effect of photothermal therapy and photodynamic therapy in the nanocomposites of MoS_2@1/3AuNRs, MoS_2@1/2AuNRs, and MoS_2@AuNRs was successfully demonstrated for an antibacterial application.

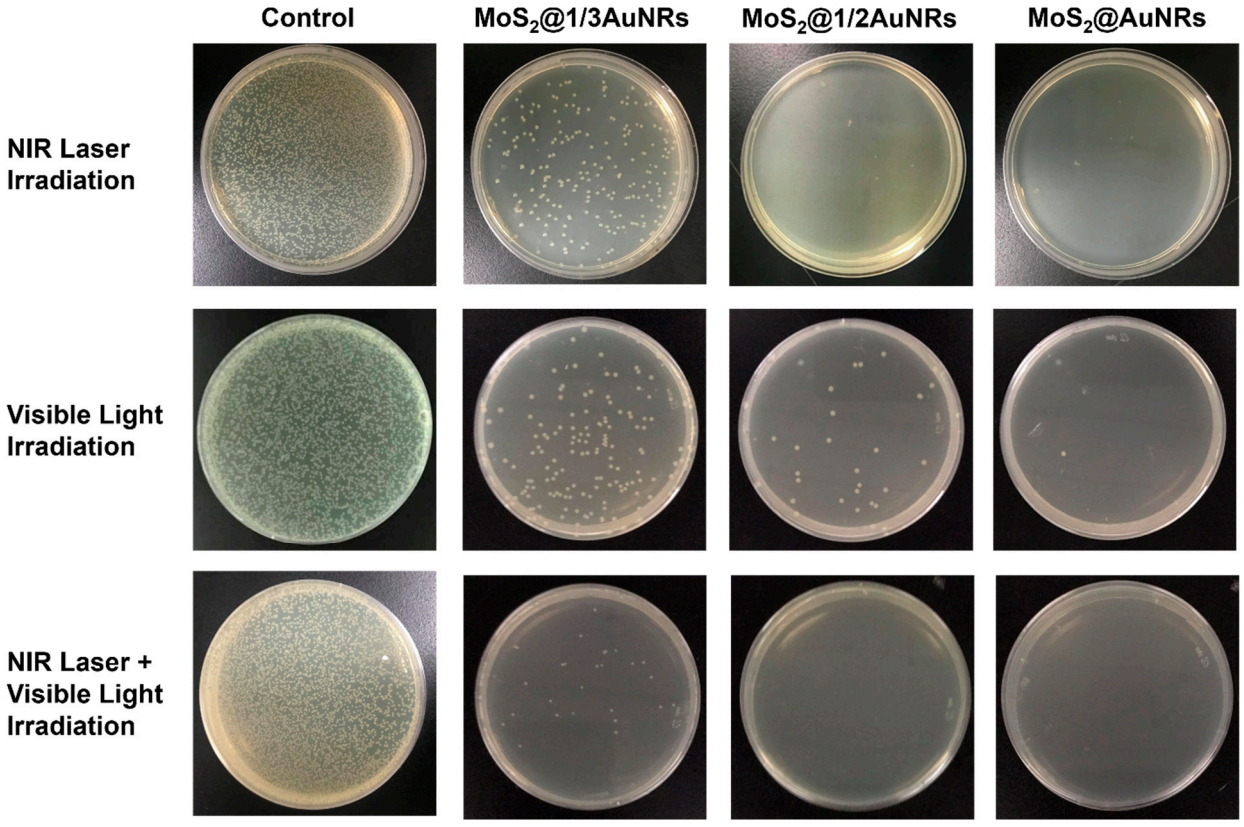

Figure 7. Photographs of the growth of *Escherichia coli* incubated with sterilized water (control) and molybdenum disulfide (MoS_2)@1/3 gold nanorods (AuNRs), MoS_2@1/2AuNRs, and MoS_2@AuNRs on LB agar plates after NIR laser, visible light, or both NIR laser and visible light irradiation. The antibacterial rate of the control was set to 0% for each type of irradiation.

4. Conclusions

In conclusion, the AuNR photothermal agent was successfully decorated onto the 1T-MoS_2 NS photodynamic agent by electrostatic adsorption to form MoS_2@AuNRs. The optical and structural properties of MoS_2@AuNRs were further demonstrated by UV–Vis spectroscopy, TEM, zeta potential, FTIR, and XRD. The photothermal performance validated that the final temperatures of MoS_2@AuNRs, MoS_2@1/2AuNRs, and MoS_2@1/3AuNRs reached 66.7, 62.9, and 59.5 °C, respectively, after 808 nm NIR laser irradiation for 10 min. For the photodynamic performance, light-induced ROS from MoS_2@AuNRs were generated mainly by the visible-light activity of 1T-MoS_2 NSs in MoS_2@AuNRs. With the combination of the AuNR photothermal agent and the 1T-MoS_2 NS photodynamic agent, the MoS_2@1/3AuNR, MoS_2@1/2AuNR, and MoS_2@AuNR nanocomposites exhibited synergistic effects of photothermal therapy and photodynamic therapy against bacteria. This work confirmed that MoS_2@AuNR nanocomposites with a superior synergistic effect of photothermal therapy and photodynamic therapy could be a promising light-activated antibacterial agent in food safety, water sterilization, antibacterial paint, and medical therapy in the near future.

Author Contributions: Conceptualization, S.Y., C.M., P.-F.C., D.I.K., F.R., H.I. and H.K.; data curation, S.Y., C.M., P.-F.C., D.I.K., F.R., H.I. and H.K.; investigation, S.Y., C.M., P.-F.C., D.I.K., F.R., H.I. and H.K.; methodology, S.Y., C.M., P.-F.C., D.I.K., F.R., H.I. and H.K.; writing—original draft, T.-R.K.; funding acquisition, T.-R.K.; project administration, T.-R.K.; resources, T.-R.K.; supervision, T.-R.K. All authors have read and agreed to the published version of the manuscript.

Funding: We thank the Ministry of Science and Technology, Taiwan (MOST 109-2113-M-038-005-MY2); Taipei Medical University; and the Higher Education Sprout Project from the Ministry of Education (MOE) in Taiwan for funding this work.

Institutional Review Board Statement: Not applicable.

Informed Consent Statement: Not applicable.

Data Availability Statement: The data presented in this study are available on request from the corresponding author.

Acknowledgments: We would like to thank Chi-Ming Lee and Chun-Chih Liu for all their help with material characterizations at the TMU Core Facility Center.

Conflicts of Interest: The authors declare no conflict of interest.

References

1. Zhu, Y.; Kuo, T.-R.; Li, Y.-H.; Qi, M.-Y.; Chen, G.; Wang, J.; Xu, Y.-J.; Chen, H.M. Emerging dynamic structure of electrocatalysts unveiled by in situ X-ray diffraction/absorption spectroscopy. *Energy Environ. Sci.* **2021**, *14*, 1928–1958. [CrossRef]
2. Tung, C.W.; Kuo, T.R.; Hsu, C.S.; Chuang, Y.; Chen, H.C.; Chang, C.K.; Chien, C.Y.; Lu, Y.J.; Chan, T.S.; Lee, J.F. Light-induced activation of adaptive junction for efficient solar-driven oxygen evolution: In situ unraveling the interfacial metal–silicon junction. *Adv. Energy Mater.* **2019**, *9*, 1901308. [CrossRef]
3. Tam, D.Y.; Zhuang, X.Y.; Wong, S.W.; Lo, P.K. Photoresponsive self-assembled DNA nanomaterials: Design, working principles, and applications. *Small* **2019**, *15*, 1805481. [CrossRef] [PubMed]
4. Li, C.-H.; Kuo, T.-R.; Su, H.-J.; Lai, W.-Y.; Yang, P.-C.; Chen, J.-S.; Wang, D.-Y.; Wu, Y.-C.; Chen, C.-C. Fluorescence-guided probes of aptamer-targeted gold nanoparticles with computed tomography imaging accesses for in vivo tumor resection. *Sci. Rep.* **2015**, *5*, 15675. [CrossRef]
5. Zhang, X.D.; Xie, X.; Wang, H.; Zhang, J.J.; Pan, B.C.; Xie, Y. Enhanced photoresponsive ultrathin graphitic-phase C_3N_4 nanosheets for bioimaging. *J. Am. Chem. Soc.* **2013**, *135*, 18–21. [CrossRef]
6. Roy, K.; Padmanabhan, M.; Goswami, S.; Sai, T.P.; Ramalingam, G.; Raghavan, S.; Ghosh, A. Graphene-MoS_2 hybrid structures for multifunctional photoresponsive memory devices. *Nat. Nanotechnol.* **2013**, *8*, 826–830. [CrossRef] [PubMed]
7. Kuo, T.-R.; Liao, H.-J.; Chen, Y.-T.; Wei, C.-Y.; Chang, C.-C.; Chen, Y.-C.; Chang, Y.-H.; Lin, J.-C.; Lee, Y.-C.; Wen, C.-Y. Extended visible to near-infrared harvesting of earth-abundant FeS_2-TiO_2 heterostructures for highly active photocatalytic hydrogen evolution. *Green Chem.* **2018**, *20*, 1640–1647. [CrossRef]
8. Kuo, T.R.; Chen, W.T.; Liao, H.J.; Yang, Y.H.; Yen, H.C.; Liao, T.W.; Wen, C.Y.; Lee, Y.C.; Chen, C.C.; Wang, D.Y. Improving hydrogen evolution activity of earth-abundant cobalt-doped iron pyrite catalysts by surface modification with phosphide. *Small* **2017**, *13*, 1603356. [CrossRef] [PubMed]

9. Hsiao, Y.C.; Jheng, P.R.; Nguyen, H.T.; Chen, Y.H.; Manga, Y.B.; Lu, L.S.; Rethi, L.; Chen, C.H.; Huang, T.W.; Lin, J.D.; et al. Photothermal-irradiated polyethyleneimine-polypyrrole nanopigment film-coated polyethylene fabrics for infrared-inspired with pathogenic evaluation. *ACS Appl. Mater. Interfaces* **2021**, *13*, 2483–2495. [CrossRef] [PubMed]
10. Lu, T.Y.; Chiang, C.Y.; Fan, Y.J.; Jheng, P.R.; Quinones, E.D.; Liu, K.T.; Kuo, S.H.; Hsieh, H.Y.; Tseng, C.L.; Yu, J.S.; et al. Dual-targeting glycol chitosan/heparin-decorated polypyrrole nanoparticle for augmented photothermal thrombolytic therapy. *ACS Appl. Mater. Interfaces* **2021**, *13*, 10287–10300. [CrossRef]
11. Mi, F.L.; Burnouf, T.; Lu, S.Y.; Lu, Y.J.; Lu, K.Y.; Ho, Y.C.; Kuo, C.Y.; Chuang, E.Y. Self-targeting, immune transparent plasma protein coated nanocomplex for noninvasive photothermal anticancer therapy. *Adv. Healthc. Mater.* **2017**, *6*, 1700181. [CrossRef]
12. Chiang, C.W.; Chuang, E.Y. Biofunctional core-shell polypyrrole-polyethylenimine nanocomplex for a locally sustained photothermal with reactive oxygen species enhanced therapeutic effect against lung cancer. *Int. J. Nanomed.* **2019**, *14*, 1575–1585. [CrossRef] [PubMed]
13. Shih, Y.H.; Luo, T.Y.; Chiang, P.F.; Yao, C.J.; Lin, W.J.; Peng, C.L.; Shieh, M.J. Egfr-targeted micelles containing near-infrared dye for enhanced photothermal therapy in colorectal cancer. *J. Control. Release* **2017**, *258*, 196–207. [CrossRef] [PubMed]
14. Liao, Y.T.; Liu, C.H.; Chin, Y.; Chen, S.Y.; Liu, S.H.; Hsu, Y.C.; Wu, K.C.W. Biocompatible and multifunctional gold nanorods for effective photothermal therapy of oral squamous cell carcinoma. *J. Mater. Chem. B* **2019**, *7*, 4451–4460. [CrossRef]
15. Chiang, C.W.; Hsiao, Y.C.; Jheng, P.R.; Chen, C.H.; Manga, Y.B.; Lekha, R.; Chao, K.M.; Ho, Y.C.; Chuang, E.Y. Strontium ranelate-laden near-infrared photothermal-inspired methylcellulose hydrogel for arthritis treatment. *Mater. Sci. Eng. C* **2021**, *123*, 111980. [CrossRef] [PubMed]
16. Satapathy, M.K.; Nyambat, B.; Chiang, C.W.; Chen, C.H.; Wong, P.C.; Ho, P.H.; Jheng, P.R.; Burnouf, T.; Tseng, C.L.; Chuang, E.Y. A gelatin hydrogel-containing nano-organic pei-ppy with a photothermal responsive effect for tissue engineering applications. *Molecules* **2018**, *23*, 1256. [CrossRef]
17. Mutalik, C.; Wang, D.-Y.; Krisnawati, D.I.; Jazidie, A.; Yougbare, S.; Kuo, T.-R. Light-activated heterostructured nanomaterials for antibacterial application. *Nanomaterials* **2020**, *10*, 643. [CrossRef] [PubMed]
18. Yougbaré, S.; Mutalik, C.; Krisnawati, D.I.; Kristanto, H.; Jazidie, A.; Nuh, M.; Cheng, T.-M.; Kuo, T.-R. Nanomaterials for the photothermal killing of bacteria. *Nanomaterials* **2020**, *10*, 1123. [CrossRef]
19. Yao, D.F.; Wang, Y.S.; Zou, R.F.; Bian, K.X.; Yuan, S.G.; Zhang, B.B.; Wang, D.B. Wavelength-adjustable butterfly molecules in dynamic nanoassemblies for extradomain-b fibronectin-modulating optical imaging and synchronous phototherapy of triple-negative breast cancer. *Chem. Eng. J.* **2021**, *420*, 127658. [CrossRef]
20. Li, J.C.; Pu, K.Y. Development of organic semiconducting materials for deep-tissue optical imaging, phototherapy and photoactivation. *Chem. Soc. Rev.* **2019**, *48*, 38–71. [CrossRef]
21. Kotagiri, N.; Sudlow, G.P.; Akers, W.J.; Achilefu, S. Breaking the depth dependency of phototherapy with cerenkov radiation and low-radiance-responsive nanophotosensitizers. *Nat. Nanotechnol.* **2015**, *10*, 370–379. [CrossRef]
22. Huang, Z.F.; Song, J.J.; Pan, L.; Zhang, X.W.; Wang, L.; Zou, J.J. Tungsten oxides for photocatalysis, electrochemistry, and phototherapy. *Adv. Mater.* **2015**, *27*, 5309–5327. [CrossRef] [PubMed]
23. Kenny, R.G.; Marmion, C.J. Toward multi-targeted platinum and ruthenium drugs—A new paradigm in cancer drug treatment regimens? *Chem. Rev.* **2019**, *119*, 1058–1137. [CrossRef]
24. Kim, S.H.; Kang, E.B.; Jeong, C.J.; Sharker, S.M.; In, I.; Park, S.Y. Light controllable surface coating for effective photothermal killing of bacteria. *ACS Appl. Mater. Interfaces* **2015**, *7*, 15600–15606. [CrossRef] [PubMed]
25. Lu, K.Y.; Jheng, P.R.; Lu, L.S.; Rethi, L.; Mi, F.L.; Chuang, E.Y. Enhanced anticancer effect of ROS-boosted photothermal therapy by using fucoidan-coated polypyrrole nanoparticles. *Int. J. Biol. Macromol.* **2021**, *166*, 98–107. [CrossRef]
26. Blair, J.M.; Webber, M.A.; Baylay, A.J.; Ogbolu, D.O.; Piddock, L.J. Molecular mechanisms of antibiotic resistance. *Nat. Rev. Microbiol.* **2015**, *13*, 42–51. [CrossRef] [PubMed]
27. Chung, C.H.; Lu, K.Y.; Lee, W.C.; Hsu, W.J.; Lee, W.F.; Dai, J.Z.; Shueng, P.W.; Lin, C.W.; Mi, F.L. Fucoidan-based, tumor-activated nanoplatform for overcoming hypoxia and enhancing photodynamic therapy and antitumor immunity. *Biomaterials* **2020**, *257*, 120227. [CrossRef]
28. Chen, C.T.; Peng, P.C.; Tsai, T.; Chien, H.F.; Lee, M.J. A novel treatment modality for malignant peripheral nerve sheath tumor using a dual-effect liposome to combine photodynamic therapy and chemotherapy. *Pharmaceutics* **2020**, *12*, 317. [CrossRef]
29. Cui, S.S.; Yin, D.Y.; Chen, Y.Q.; Di, Y.F.; Chen, H.Y.; Ma, Y.X.; Achilefu, S.; Gu, Y.Q. In vivo targeted deep-tissue photodynamic therapy based on near-infrared light triggered upconversion nanoconstruct. *ACS Nano* **2013**, *7*, 676–688. [CrossRef] [PubMed]
30. Zhou, Z.J.; Song, J.B.; Nie, L.M.; Chen, X.Y. Reactive oxygen species generating systems meeting challenges of photodynamic cancer therapy. *Chem. Soc. Rev.* **2016**, *45*, 6597–6626. [CrossRef]
31. Lebedev, A.; Anariba, F.; Tan, J.C.; Li, X.; Wu, P. A review of physiochemical and photocatalytic properties of metal oxides against *Escherichia coli*. *J. Photochem. Photobiol. A* **2018**, *360*, 306–315. [CrossRef]
32. Liu, S.; Pan, X.T.; Liu, H.Y. Two-dimensional nanomaterials for photothermal therapy. *Angew. Chem. Int. Ed.* **2020**, *59*, 5890–5900. [CrossRef] [PubMed]
33. Hu, R.Z.; Fang, Y.; Huo, M.F.; Yao, H.L.; Wang, C.M.; Chen, Y.; Wu, R. Ultrasmall $Cu_{2-X}S$ nanodots as photothermal-enhanced fenton nanocatalysts for synergistic tumor therapy at nir-II biowindow. *Biomaterials* **2019**, *206*, 101–114. [CrossRef]
34. Liu, Y.J.; Bhattarai, P.; Dai, Z.F.; Chen, X.Y. Photothermal therapy and photoacoustic imaging via nanotheranostics in fighting cancer. *Chem. Soc. Rev.* **2019**, *48*, 2053–2108. [CrossRef] [PubMed]

35. Yougbaré, S.; Chou, H.-L.; Yang, C.-H.; Krisnawati, D.I.; Jazidie, A.; Nuh, M.; Kuo, T.-R. Facet-dependent gold nanocrystals for effective photothermal killing of bacteria. *J. Hazard. Mater.* **2021**, *407*, 124617. [CrossRef]
36. Zhao, Y.-Q.; Sun, Y.; Zhang, Y.; Ding, X.; Zhao, N.; Yu, B.; Zhao, H.; Duan, S.; Xu, F.-J. Well-defined gold nanorod/polymer hybrid coating with inherent antifouling and photothermal bactericidal properties for treating an infected hernia. *ACS Nano* **2020**, *14*, 2265–2275. [CrossRef]
37. Tian, Q.; Wang, Q.; Yao, K.X.; Teng, B.; Zhang, J.; Yang, S.; Han, Y. Multifunctional polypyrrole@Fe_3O_4 nanoparticles for dual-modal imaging and in vivo photothermal cancer therapy. *Small* **2014**, *10*, 1063–1068. [CrossRef]
38. Yang, X.; Xia, P.; Zhang, Y.; Lian, S.; Li, H.; Zhu, G.; Wang, P. Photothermal nano-antibiotic for effective treatment of multidrug-resistant bacterial infection. *ACS Appl. Bio Mater.* **2020**, *3*, 5395–5406. [CrossRef]
39. Liu, C.; Kong, D.; Hsu, P.-C.; Yuan, H.; Lee, H.-W.; Liu, Y.; Wang, H.; Wang, S.; Yan, K.; Lin, D. Rapid water disinfection using vertically aligned MoS_2 nanofilms and visible light. *Nat. Nanotechnol.* **2016**, *11*, 1098–1104. [CrossRef] [PubMed]
40. Karunakaran, S.; Pandit, S.; Basu, B.; De, M. Simultaneous exfoliation and functionalization of 2H-MoS_2 by thiolated surfactants: Applications in enhanced antibacterial activity. *J. Am. Chem. Soc.* **2018**, *140*, 12634–12644. [CrossRef]
41. Yougbare, S.; Chang, T.-K.; Tan, S.-H.; Kuo, J.-C.; Hsu, P.-H.; Su, C.-Y.; Kuo, T.-R. Antimicrobial gold nanoclusters: Recent developments and future perspectives. *Int. J. Mol. Sci.* **2019**, *20*, 2924. [CrossRef]
42. Chang, T.-K.; Cheng, T.-M.; Chu, H.-L.; Tan, S.-H.; Kuo, J.-C.; Hsu, P.-H.; Su, C.-Y.; Chen, H.-M.; Lee, C.-M.; Kuo, T.-R. Metabolic mechanism investigation of antibacterial active cysteine-conjugated gold nanoclusters in *Escherichia coli*. *ACS Sustain. Chem. Eng.* **2019**, *7*, 15479–15486. [CrossRef]
43. Tsai, T.; Chien, H.F.; Wang, T.H.; Huang, C.T.; Ker, Y.B.; Chen, C.T. Chitosan augments photodynamic inactivation of gram-positive and gram-negative bacteria. *Antimicrob. Agents Chemother.* **2011**, *55*, 1883–1890. [CrossRef]
44. Tsai, T.; Yang, Y.T.; Wang, T.H.; Chien, H.F.; Chen, C.T. Improved photodynamic inactivation of gram-positive bacteria using hematoporphyrin encapsulated in liposomes and micelles. *Lasers Surg. Med.* **2009**, *41*, 316–322. [CrossRef] [PubMed]
45. Chen, C.P.; Chen, C.T.; Tsai, T.M. Chitosan nanoparticles for antimicrobial photodynamic inactivation: Characterization and in vitro investigation. *Photochem. Photobiol.* **2012**, *88*, 570–576. [CrossRef]
46. Mutalik, C.; Krisnawati, D.I.; Patil, S.B.; Khafid, M.; Atmojo, D.S.; Santoso, P.; Lu, S.-C.; Wang, D.-Y.; Kuo, T.-R. Phase-dependent MoS_2 nanoflowers for light-driven antibacterial application. *ACS Sustain. Chem. Eng.* **2021**, *9*, 7904–7912. [CrossRef]
47. Mutalik, C.; Hsiao, Y.-C.; Chang, Y.-H.; Krisnawati, D.I.; Alimansur, M.; Jazidie, A.; Nuh, M.; Chang, C.-C.; Wang, D.-Y.; Kuo, T.-R. High uv-vis-nir light-induced antibacterial activity by heterostructured TiO_2-FeS_2 nanocomposites. *Int. J. Nanomed.* **2020**, *15*, 8911. [CrossRef] [PubMed]
48. Ahmad, A.; Ullah, S.; Ahmad, W.; Yuan, Q.; Taj, R.; Khan, A.U.; Rahman, A.U.; Khan, U.A. Zinc oxide-selenium heterojunction composite: Synthesis, characterization and photo-induced antibacterial activity under visible light irradiation. *J. Photochem. Photobiol. B Biol.* **2020**, *203*, 111743. [CrossRef] [PubMed]
49. Yang, Z.; Hao, X.; Chen, S.; Ma, Z.; Wang, W.; Wang, C.; Yue, L.; Sun, H.; Shao, Q.; Murugadoss, V. Long-term antibacterial stable reduced graphene oxide nanocomposites loaded with cuprous oxide nanoparticles. *J. Colloid Interface Sci.* **2019**, *533*, 13–23. [CrossRef]
50. Castellanos-Gomez, A.; Quereda, J.; van der Meulen, H.P.; Agraït, N.; Rubio-Bollinger, G. Spatially resolved optical absorption spectroscopy of single-and few-layer MoS_2 by hyperspectral imaging. *Nanotechnology* **2016**, *27*, 115705. [CrossRef]
51. Kuo, T.-R.; Hovhannisyan, V.A.; Chao, Y.-C.; Chao, S.-L.; Chiang, S.-J.; Lin, S.-J.; Dong, C.-Y.; Chen, C.-C. Multiple release kinetics of targeted drug from gold nanorod embedded polyelectrolyte conjugates induced by near-infrared laser irradiation. *J. Am. Chem. Soc.* **2010**, *132*, 14163–14171. [CrossRef]
52. Jeon, H.B.; Tsalu, P.V.; Ha, J.W. Shape effect on the refractive index sensitivity at localized surface plasmon resonance inflection points of single gold nanocubes with vertices. *Sci. Rep.* **2019**, *9*, 13635. [CrossRef]
53. Yan, D.; Liu, X.; Deng, G.; Yuan, H.; Wang, Q.; Zhang, L.; Lu, J. Facile assembling of novel polypyrrole nanocomposites theranostic agent for magnetic resonance and computed tomography imaging guided efficient photothermal ablation of tumors. *J. Colloid Interface Sci.* **2018**, *530*, 547–555. [CrossRef] [PubMed]
54. Chen, H.; Liu, Z.; Li, S.; Su, C.; Qiu, X.; Zhong, H.; Guo, Z. Fabrication of graphene and aunp core polyaniline shell nanocomposites as multifunctional theranostic platforms for SERS real-time monitoring and chemo-photothermal therapy. *Theranostics* **2016**, *6*, 1096. [CrossRef]
55. Feng, W.; Chen, L.; Qin, M.; Zhou, X.; Zhang, Q.; Miao, Y.; Qiu, K.; Zhang, Y.; He, C. Flower-like pegylated MoS_2 nanoflakes for near-infrared photothermal cancer therapy. *Sci. Rep.* **2015**, *5*, 17422. [CrossRef] [PubMed]
56. Truong, P.L.; Cao, C.; Park, S.; Kim, M.; Sim, S.J. A new method for non-labeling attomolar detection of diseases based on an individual gold nanorod immunosensor. *Lab Chip* **2011**, *11*, 2591–2597. [CrossRef]
57. Patil, S.B.; Chou, H.-L.; Chen, Y.-M.; Hsieh, S.-H.; Chen, C.-H.; Chang, C.-C.; Li, S.-R.; Lee, Y.-C.; Lin, Y.-S.; Li, H. Enhanced N_2 affinity of 1T-MoS_2 with a unique pseudo-six-membered ring consisting of N–Li–S–Mo–S–Mo for high ambient ammonia electrosynthesis performance. *J. Mater. Chem. A* **2021**, *9*, 1230–1239. [CrossRef]
58. Samim, M.; Prashant, C.; Dinda, A.; Maitra, A.; Arora, I. Synthesis and characterization of gold nanorods and their application for photothermal cell damage. *Int. J. Nanomed.* **2011**, *6*, 1825. [CrossRef] [PubMed]
59. Abareshi, A.; Pirlar, M.A.; Houshiar, M. Experimental and theoretical investigation of the photothermal effect in gold nanorods. *New J. Chem.* **2021**, *45*, 298–303. [CrossRef]